Results in Physics 30 (2021) 104897

Contents lists available at ScienceDirect

Results in Physics

journal homepage: www.elsevier.com/locate/rinp

Tapered depressed-cladding waveguide lasers modulated by Ag nanoparticles embedded in SiO_2

Shuo Sun [a], Xiaoli Sun [a,*], Feng Ren [b], Carolina Romero [c], Javier R. Vázquez de Aldana [c,d], Yuechen Jia [a,*], Feng Chen [a]

[a] School of Physics, State Key Laboratory of Crystal Materials, Shandong University, Jinan 250100, China
[b] Department of Physics, Center for Ion Beam Application and Center for Electron Microscopy, Wuhan University, Wuhan 430072, China
[c] Group de investigación en Aplicaciones del Láser y Fotónica, Universidad de Salamanca, PL. La Merced SN, 37008 Salamanca, Spain
[d] Spanish Center for Pulsed Lasers, M5 Bldg. Science Park, 37185 Villamayor, Salamanca, Spain

ARTICLE INFO

Keywords:
Tapered depressed-cladding waveguide
Q-switched mode-locked laser
Ag:SiO_2
Femtosecond laser direct writing
Optical waveguides

ABSTRACT

We report on fabrication of tapered circular depressed-cladding waveguides in Nd:YAG crystal by femtosecond laser direct writing (FsLDW). Based on the fabricated waveguides, for the first time to the best of our knowledge, efficient *Q*-switched mode-locked (QML) lasers are realized by employing silver nanoparticles (NPs) embedded in fused silica as saturable absorber (SA) element. Laser pulses as short as 25 ps with a repetition rate of 7.7 GHz are generated at a wavelength of 1064 nm. We systematically explore the influence of incident-output facet and the reduction factors on guiding properties and laser performance by conducting a comparative study of different tapers, and it has been found that the waveguides with tapered structures can suppress multi-mode guiding while ensure fundamental-mode output for waveguide lasers. Our work paves a new way toward developing three-dimensional (3D) waveguide for applications in on-chip ultrafast laser sources.

Introduction

Photonic integrated circuits (PICs) play an essential role in modern optical fiber communications, spectral sensors and quantum information processing [1–3]. In particular, three-dimensional (3D) PICs have been used in many applications due to their flexibility and versatility in design freedom, including large-scale crossing-free optical switching matrices, 3D optical phased arrays for LIDAR, 3D docking couplers for micro-nano 3D printing and more recently 3D optical waveguides [4–6]. Therefore, the design and application of novel 3D photonic devices have become an inevitable trend. Benefiting from its advantages of high processing precision, 3D writing and wide application range of materials compared to lithographic methods, dicing, ablation, etching and so on [5–9], femtosecond laser direct writing (FsLDW) has been developed as an important technology in the research of 3D micromachining in recent years [10–13]. Compared with bulk lasers, depressed waveguides with a quasi-continuous low-index potential barrier defined by FsLDW can guide optical wave propagation in the crystal and meanwhile control the modal behavior [12–16]. Furthermore, depressed cladding waveguides, which enable flexible integration with optical fiber and better confinement of light field, have been extensively employed in construction of various functional devices [17]. Therefore, designing different depressed waveguide structures to realize stable and high-efficiency pulsed lasers is of great significance for developing on-chip integrated photonics devices. Fabrication of fiber-shaped depressed-cladding waveguide, tunnel-shaped single-line waveguide and double-line waveguide over the past few years has gradually developed into a mature technology [11–14,18]. However, the application of more complex and novel 3D cladding waveguide structures is rarely reported due to the challenges of ensuring the continuity and smoothness of the waveguide structure while avoiding the crystal cracking in the complex FsLDW process [18–20].

High-order modes would lead to severe competition with low-order modes and energy dispersion in pulsed lasers, and in turn to laser performance instability [21,22]. With a view to improving the laser performance, it is very crucial to suppress high-order modes to ensure the ideal state of single-mode operation. To this end, waveguides with tapered structures have been found to have the potential to control the modal behavior of the output laser due to their special geometries in which the cross-sectional size decreases along the guided wave

* Corresponding authors.
E-mail addresses: xlsun@sdu.edu.cn (X. Sun), yuechen.jia@sdu.edu.cn (Y. Jia).

https://doi.org/10.1016/j.rinp.2021.104897
Received 1 August 2021; Received in revised form 31 August 2021; Accepted 7 October 2021
Available online 8 October 2021

propagation direction [21,23–25]. The demonstrated work so far focused mainly on the fabrication parameters and basic optical characterization in the continuous-wave (CW) regime. Taking advantage of tapered depressed cladding waveguide, we foresee that it has the potential to be a gain medium to realize high-efficiency pulsed laser.

Due to the significance of saturable absorbers (SAs) in ultrashort pulse lasers, the pace of research on novel and ultrafast SA materials has never stopped in the last few years [26–30]. It has been demonstrated that metallic nanoparticles (NPs) exhibit the fascinating abilities to modulate the nonlinear optical response of dielectric materials benefiting from the excellent localized surface plasmon resonance effect [31,32]. By applying ion implantation technology, dielectric optical crystals with embedded noble metallic NPs, which have been proven to be excellent SAs, have remarkable properties for enhancing surrounding electromagnetic field [33–35]. Excited by their unique characteristics such as the broad-band transparency, excellent thermal resistance and high stability [36,37], a number of studies on SiO2-based materials have been reported including serving as substrates for synthesizing metallic NPs [38,39]. As an example, Li *et al.* have demonstrated that embedding the Ag NPs into SiO_2 (Ag:SiO_2) can substantially enhance the third-order nonlinear optical (NLO) responses of insulating SiO_2 [32]. Based on the Ag:SiO_2 as an SA, a passively *Q*-switched mode-locked (QML) operation has been achieved, offering a good choice for ultrafast SA.

In this work, tapered depressed cladding waveguide is used as gain medium to realize high-efficiency picosecond pulsed laser. We design three types of tapered depressed-cladding waveguides by FsLDW with tapered cladding radii of 15–10 μm, 20–10 μm and 25–10 μm at the incident-output facet. The corresponding reduction factors are 1.5:1, 2:1, and 2.5:1, respectively. The guiding and lasing performance of three tapered waveguides in the CW and QML operations are comparatively analyzed. As far as we know, this is the first demonstration of QML operation based on a tapered depressed cladding waveguide successfully, paving a new path towards designing and optimization of waveguide configurations for high-efficiency pulsed lasers with compact geometries.

Sample preparation and characterization

Depressed tapered cladding waveguide fabrication

We use a Nd:YAG (1 at.% Nd^{3+} ions) crystal wafer with the dimension of 20 × 10 × 2 mm^3 in this work with all the crystal facets well-polished to an optical level. The definition of the tapered depressed-cladding waveguide in this work exploits the method of FsLDW. The femtosecond laser system used for waveguide fabrication is a Ti:Sapphire based regenerative amplifier (Spitfire, Spectra Physics, Santa Clara), which delivers 795-nm linearly polarized pulses with a maximum energy of 1 mJ per pulse and a pulse duration of 120 fs at a repetition rate of 1 kHz. The fabrication process of tapered depressed waveguides is schematically illustrated in Fig. 1(a). By using a 40 × microscope objective (N.A. = 0.65), the incident laser beam is focused beneath the crystal surface at a maximum focus depth of 150 μm. The sample is set on a three-axis (*XYZ*) motorized stage that translates precisely at a constant velocity of 500 μm/s relative to the femtosecond laser beam by a Turbo Pmac controller (Delta Tau systems, Chatsworth).

As indicated in Fig. 1(d), the tapered waveguide is formed by three waveguide structures including two straight waveguides at the input and the output sections and a truncated-like cone in the middle connecting them. The laser damage tracks with the same separation of "*d*" define the circular profile of the waveguide cross section. The separation *d* between the damage tracks in the cladding is smoothly decreased from d_{max} to d_{min}, thus linearly decreasing the waveguide radius along the propagation direction. The optimum FsLDW conditions for Nd:YAG waveguide formation and the method for determining d_{max} and d_{min} have been demonstrated in detail in the previous report [21]. To avoid crystal cracking in the fabrication process while maintaining a good light confinement, d_{max} and d_{min} are determined to be 4 and 2 μm in this work, resulting in the reduction factor of 2:1. In order to achieve a larger reduction factor within the separation range of 2–4 μm, an effective strategy is reducing the quantity of FsLDW tracks when the separation *d* reaches to the minimum d_{min}, forming WG3 with a reduction factor of 2.5:1 (see Fig. 1(e)). As shown in Fig. 1(b), the radius of the cladding is continuously decreased from R_{in} to R_{out} (15 μm, 20 μm, 25 μm for R_{in} and 10 μm for R_{out} in all cases). The radii R_{in} and R_{out} satisfy the following linear function,

$$\theta = arctan\left(\frac{R_{in} - R_{out}}{L}\right) \quad (1)$$

where *L* is the length of the tapered section in the middle. In our fabrication process, the *L* of all tapered waveguides is designed to be 8 mm and the lengths of straight waveguide sections at both ends are 1 mm.

The optical microscopic images of the input and output end-facets of tapered waveguides are shown in Fig. 1(c). The purpose of this tapered structure with a large radius at the input and a minor radius at the output is to improve the coupling efficiency of the external source while maintaining single-mode output for high-efficiency lasing operation.

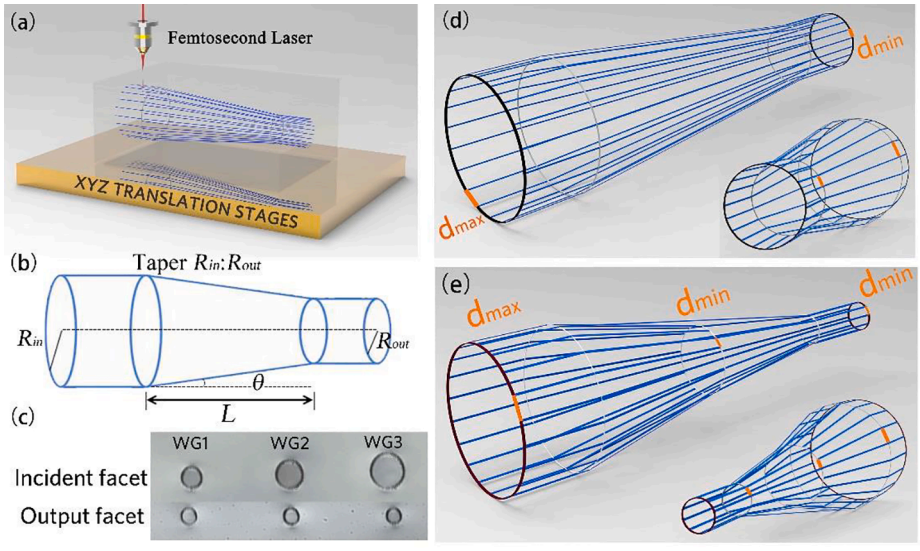

Fig. 1. (a) Schematical illustration of FsLDW tapered waveguide fabrication in Nd:YAG. (b) Schematic illustration of a tapered waveguide with the incident and output cladding radius of R_{in} and R_{out}, respectively. (c) Optical microscope cross-sectional image of the input and output facets of FsLDW waveguides (WG1-WG3). (d) The laser manufacturing prototype model of the tapered cladding with reduction factor d_{max}:d_{min} of 2:1. (e) The laser manufacturing model of the tapered cladding with the reduction factor d_{max}:d_{min} of 4:1 by further decreasing the quantity of tracks. The insets are the corresponding side views.

Waveguiding properties

The optical guiding performance of three tapered waveguides are investigated through an end-facet coupling system. The laser centered at 1064 nm is emitted by a linearly polarized CW solid-state laser. The propagation loss α is calculated by the following formula

$$\alpha = -10\mathrm{Log}\left(\frac{P_{out}}{P_{in}}\right) \quad (2)$$

where P_{out} and P_{in} are the output and input power, respectively. The propagation losses of WG1-WG3 at TE and TM polarizations after calculation are summarized in Table 1. The waveguide structure with an input radius of 20 μm (WG2) exhibits the lowest propagation losses of 4.07 dB/cm at TE polarization and 4.40 dB/cm at TM polarization. As for the depressed-cladding waveguide, the propagation loss mainly originates from the light scattering of the rough boundary introduced by the FsLDW. The larger-size cladding waveguide generates higher output power since the input light would be better coupled to the waveguide and its boundary region is relatively far away from the optical modes. As a result, the propagation loss decreases as the radius of input cladding increases. Here, the influence of size can also be regarded as the influence of the reduction factor of R_{in}:R_{out} in this work as all the R_{out} are the same. However, WG3 with a larger input cladding size exhibits a slightly higher propagation loss comparing with WG2, probably because 8-mm length is relatively short in case of such a high reduction factor (2.5:1) and thus resulting in a steep mode transformation.

In addition, the polarization-dependency of WG1-WG3 guiding properties is obtained by measuring the output power while adjusting the polarization angles at a constant incident power. The all-angle light propagation loss of each waveguide at 1064 nm is shown in Fig. 2. It can be found that the optical guiding property is polarization-dependent. This is most probably caused by the slight difference in the focusing laser energy at different depths beneath the Nd:YAG sample surface, resulting in different refractive index changes and polarization-dependent guiding properties. The propagation loss reaches minimum at the polarization angles of 90° and 270° (corresponding to the TE polarization in both cases), suggesting a good guidance property along TE polarization.

Ag:SiO_2 nanoparticles characterization

The Ag:SiO_2 SA sample is prepared by direct Ag ion implantation (with a fluence of 7.8×10^{16} ions/cm^2 and an energy of 120 keV), by which a Ag-NP monolayer embedded in SiO_2 is formed (similar work on the fabrication of Ag:SiO_2 SA was reported in [32]). In order to investigate the physical properties of Ag NPs, the atomic number contrast imaging by HAADF-STEM as the high-resolution transmission electron microscope (HRTEM) is carried out. The HRTEM image derived from Fig. 3(a) exhibits the polycrystalline state with a lattice spacing of 2.3 Å.

In order to better investigate the nonlinear optical response of the Ag:SiO_2 and verify its potential for ultrafast SA, the open-aperture *Z*-scan experiment is performed. A femtosecond ytterbium fiber mode-locked laser (FemtoYL-10, YSL Photonics, China) with a tunable repetition rate (25-kHz to 5-MHz) and 400-fs temporal duration at 1030 nm is employed as the laser excitation source. The laser beam is focused on the Ag:SiO_2 sample with a beam waist radius of 52 μm. During the measurement, the Ag:SiO_2 sample is placed on a PC-controlled translation stage such that the moving step and velocity along the *Z*-axis can

Table 1
Waveguide propagation losses of WG1-WG3 at 1064 nm.

	WG1	WG2	WG3
TE (dB/cm)	4.26	4.07	4.10
TM (dB/cm)	4.61	4.40	4.45

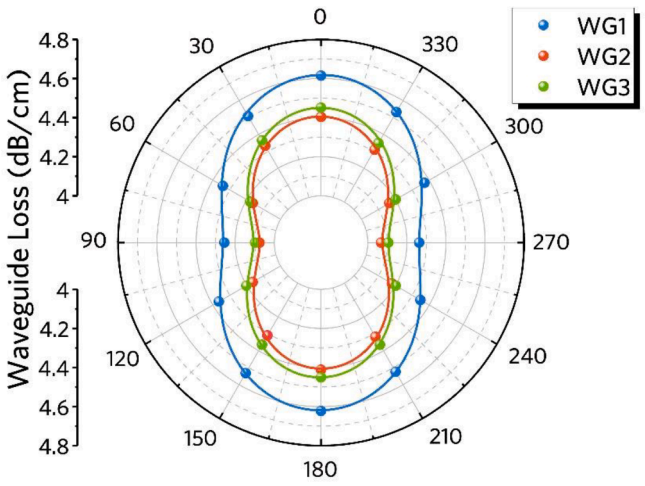

Fig. 2. Waveguide loss as a function of all-angle light transmission of WG1-WG3.

be controlled. The real-time powers of the Ag:SiO_2 sample at different positions of the reference and transmitted light are detected simultaneously by two detectors.

Fig. 3(c) indicates the *Z*-scan measurement curves with normalized transmittance as a function of the sample position. The transmittance gradually increases as the increase of laser power density. With a good symmetry centered at $Z = 0$ position, an apparent peak is produced at the focal point position, thus indicating an excellent typical saturable absorption characteristic of the Ag:SiO_2 sample. For the purpose of studying more detailed information, the saturation intensity I_s and the modulation depth ΔR are estimated by fitting the experimental data according to the nonlinear absorption model using following formula,

$$T = \left(1 - \frac{\Delta \mathrm{RI}_s}{I_s + \frac{I_0}{1+Z^2/Z_0^2}}\right) \Big/ (1 - \Delta \mathrm{R}) \quad (3)$$

where T is the normalized transmittance, ΔR is the modulation depth, I_s is the saturation intensity, I_0 is the incident peak intensity and Z_0 is the Rayleigh length of incident beam. By fitting the obtained data, ΔR and I_s of the Ag:SiO_2 sample are determined to be approximately 7.1% and 6.3 mJ/cm^2, respectively. In order to further discuss the nonlinear optical response of the sample, the transmittance as a function of the excitation laser intensity is also measured and fitted (see Fig. 3(d)).

QML laser operation

The lasing performance of the tapered Nd:YAG waveguides at pulsed regime is further investigated by incorporating Ag:SiO_2 sample into the waveguide cavity as SA (the schematical illustration of pulsed waveguide laser experiment is shown in Fig. 4). The pump source is a tunable Ti:sapphire laser (Coherent MBR-PE) emitting linearly polarized light at 808 nm. The polarization of the incident laser is controlled by a half-wave plate. To implement a better optical coupling, a spherical convex lens ($f = 25$ mm) is used. The input mirror is a flat mirror, which has an antireflection coating at 808 nm and a high reflectivity at 1064 nm. The output mirror is high-reflection coated at 1064 nm. A compact Fabry-Pérot cavity is formed by clamping the Nd:YAG crystal waveguide and SA tightly between the in- and out-put mirror through a cage system. After optimization, the physical length of the cavity is around 10.9 mm. An 850-nm long-pass filter is used to filter out the residual laser. The performance of pulsed laser is evaluated using a 25-GHz wide-bandwidth real time digital oscilloscope (Tektronix, MSO 72504DX). For this purpose, a 20 × microscope objective (N.A. = 0.4) is used to

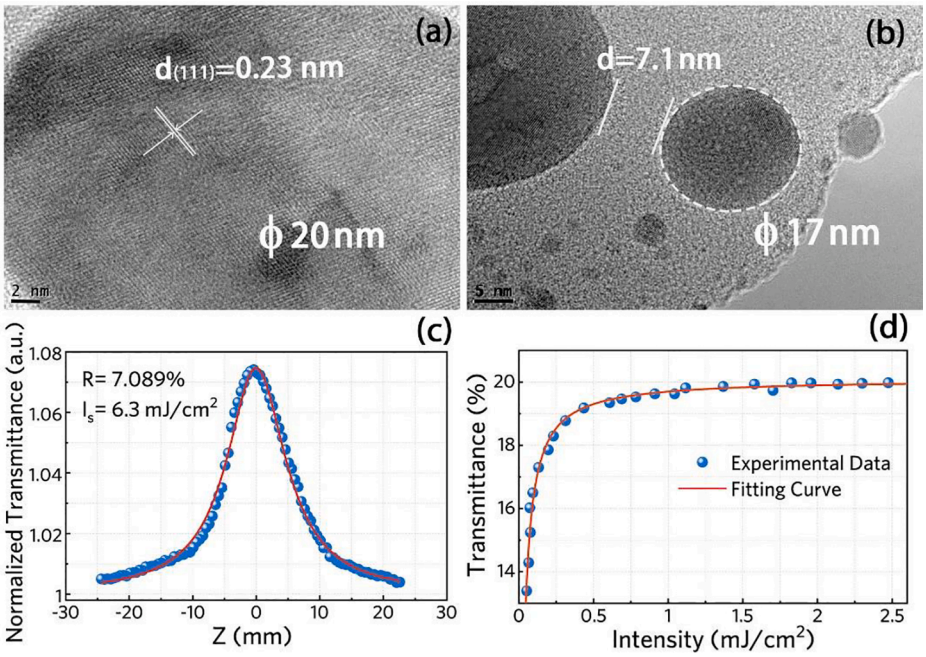

Fig. 3. The HRTEM images of (a) the single NP and (b) the interparticle spacing. (c) The open-aperture *Z*-scan measurement and (d) the nonlinear transmittance curve of Ag:SiO_2 SA. The scatters are experimental data and solid lines are the fitting curves.

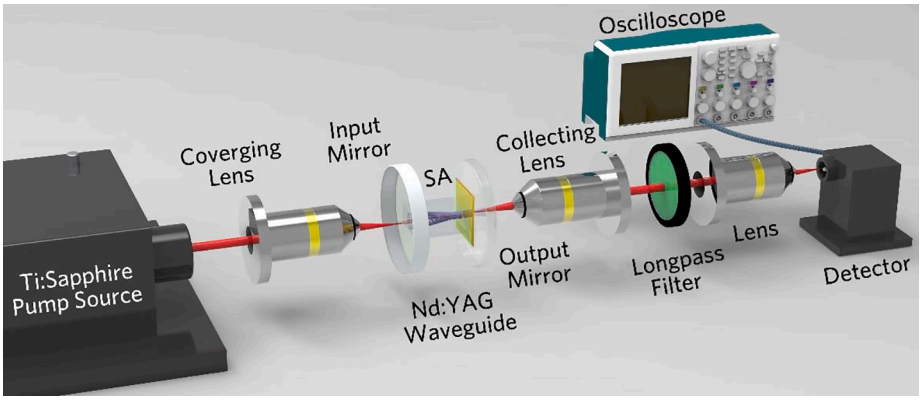

Fig. 4. The QML experimental set-up based on the Ag:SiO_2 SA.

better couple the filtered output laser into a high-speed InGaAs photodetector (New Focus, 1414 model), which is connected to the oscilloscope to observe the pulse sequence.

After inserting the Ag:SiO_2 sample as a SA, a QML operation is obtained at 1 μm based on Nd:YAG tapered cladding waveguides. Fig. 5(a) and (b) depict the average output power of QML operation for three tapered waveguides as a function of the incident power. For TE(TM) polarization, the maximum output power values are determined to be 77.6 mW (57.4 mW), 91.5 mW (70.7 mW), and 68.4 mW (48.4 mW) for WG1, WG2 and WG3 at the pump power of 910 mW, respectively. The pulsed laser generation based on WG3 has a higher lasing threshold, which could be attributed to its higher propagation loss. Table 2 summarizes the QML performance of all the waveguides. WG2 shows the highest slope efficiency, output power and optical-to-optical conversion efficiency along both TE and TM polarizations.

In general, the depressed-cladding waveguide with a large size is supposed to exhibit multimode output since the cladding defects result in the energy transfer to higher-order modes. However, it is clear from Fig. 5(c) that all the QML modes have single-mode profiles, demonstrating the superior capability of tapered waveguide for suppressing the generation of higher-order modes. It can be seen that the output laser based on WG3 exhibits a relatively inferior laser mode with an unsmooth mode border. This may be attributed to the decreased tracks quantity in the fabrication process of WG3, leading to a weakened optical confinement. In addition, the current taper length *L* is relatively short with a larger reduction factor for WG3 such that it is difficult to achieve efficient quasi-adiabatic mode transformation from an excited input multimode into a single-mode operation completely in pulse lasers. The laser emission spectrum is centered at 1064 nm as shown in the left inset in Fig. 5(a).

Furthermore, the variation of output power under different polarization angles is indicated in Fig. 5(d) with a fixed launched power of 620 mW. The clear polarization-dependent effect with better lasing performance along TE polarization is observed, which is in good agreement with the variation of propagation loss in Fig. 2.

Owing to the comparatively poor laser performance of WG3, it is difficult to obtain a stable QML operation. The typical *Q*-switched envelope that consists of plenty of mode-locked pulses based on WG1 and WG2 with pulse durations of 38 ns and 49 ns (under the maximum pump power of 910 mW), respectively, are illustrated in Fig. 6(a) and (e). The following Fig. 6(b) and (f) indicate the corresponding mode-locked pulse trains on the timescale of 400 ps/div. The fundamental repetition

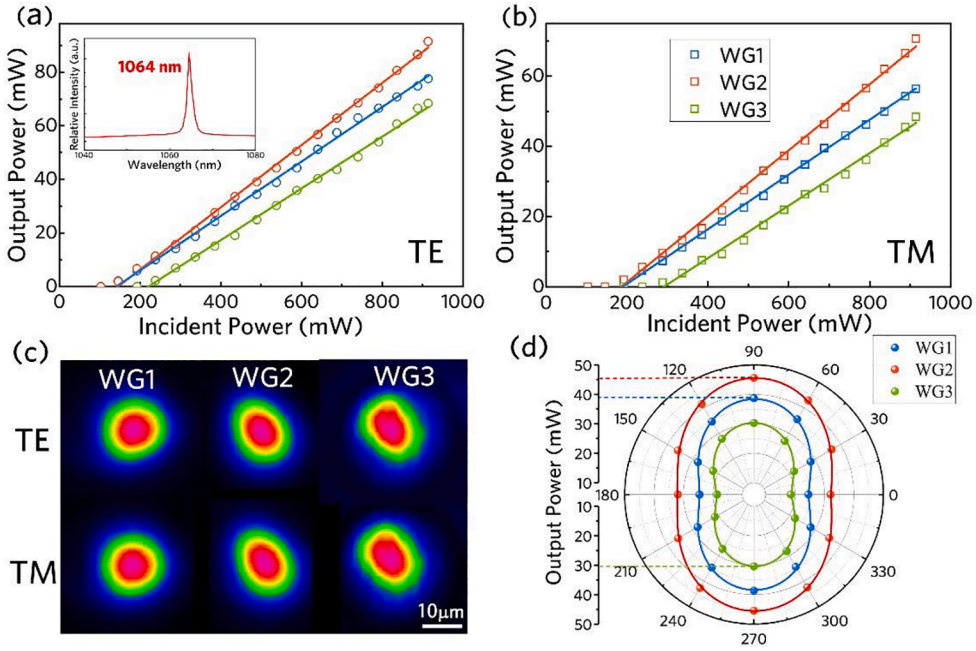

Fig. 5. Output power as a function of incident power at (a) TE polarization with a left inset of the laser emission spectrum modulated by Ag:SiO_2 and (b) TM polarization, together with (c) the corresponding laser modes for WG1-WG3. (d) Output power as a function of all-angle light transmission at a fixed launched power.

Table 2
Laser performance summarized from Fig. 5.

	Slope efficiency	Maximum output power (mW)	Optical-to-optical conversion efficiency
	TE (TM)	TE (TM)	TE (TM)
WG1	10.2% (7.8%)	77.6 (56.4)	8.5% (6.2%)
WG2	11.6% (9.4%)	91.5 (70.7)	10.0% (7.7%)
WG3	9.6% (7.5%)	68.4 (48.4)	7.5% (5.3%)

frequency is estimated to be ~ 7.64 GHz in this experiment by considering the waveguide cavity length and Nd:YAG refractive index, which is roughly in accordance with the experimental results. In order to study the QML stability, the radio frequency (RF) spectrum of the laser pulses are recorded as shown in Fig. 6(d) and (h), showing the signal-to-noise ratio (SNR) of about 50 dB. And the performance of such a waveguide QML maintains at the same level in hours of measurement. It can be seen that the QML operation of both WG1 and WG2 exhibits excellent performance, suggesting the potential applications of tapered waveguides in pulsed lasers. The pulse duration of WG1 (38 ns for *Q*-switched pulses and 25 ps for mode-locked pulses) is slightly superior than that of WG2 due to its better beam quality and higher intracavity intensity caused by the smaller input size in the laser cavity of WG1. Although WG2 with a larger input size is beneficial for increasing output power, the superior beam quality of WG1 elevates the laser performance operated in the pulsed regime. Therefore, it can be concluded that excellent pulsed lasers based on tapered waveguides require both sufficiently large input cladding and optimized taper length. This is as far as we know the first demonstration of QML based on Nd:YAG tapered depressed-cladding waveguide. Moreover, 25-ps mode-locked pulse is so far the shortest pulse duration for any type of *Q*-switched mode-locked waveguide lasers modulated by employing Ag:SiO_2 SA.

Conclusion

In conclusion, tapered depressed cladding waveguide has been fabricated by FsLDW in Nd:YAG crystal and used as gain medium to generate stable QML operation with good beam quality. All the tapered waveguides exhibit excellent capability of manipulating optical modes in terms of achieving single-mode behavior. The application and

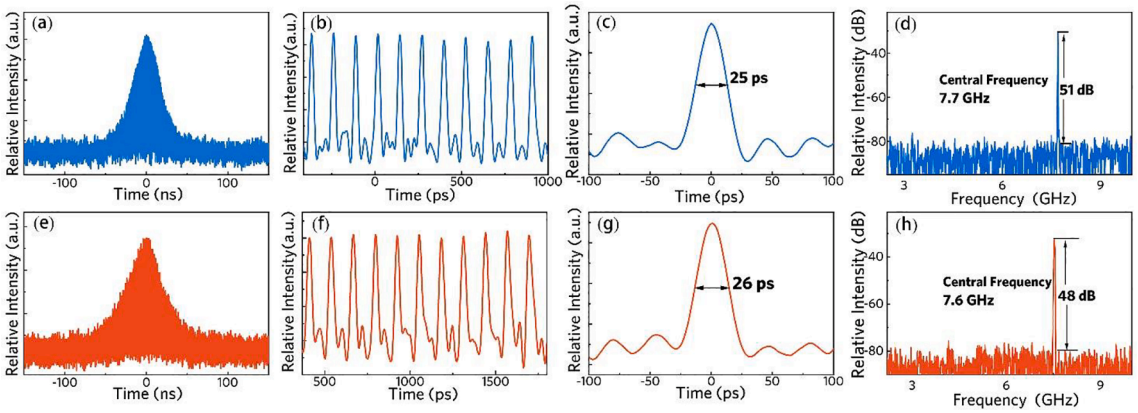

Fig. 6. Q-switched envelope on a nanosecond scale, mode-locked pulse trains on picosecond timescale, single pulse profile of the output laser, and the RF spectrum for (a), (b), (c), (d) WG1 and (e), (f), (g), (h) WG2, respectively.

exploration of 3D tapered waveguides in the pulsed regime evidences the enormous potential for the improvement of laser performance in the field of ultrafast pulsed lasers.

Funding

National Natural Science Foundation of China (12074223, 1210040430); Taishan Scholar Foundation of Shandong Province; Qilu Young Scholar Program of Shandong University; China Postdoctoral Science Foundation (2020M682155); Consejería de Educación, Junta de Castilla y León (SA287P18, SA136P20); Ministerio de Economía y Competitividad (FIS2017-87970R).

CRediT authorship contribution statement

Shuo Sun: Data curation, Investigation, Software, Writing – original draft. **Xiaoli Sun:** Conceptualization, Formal analysis, Funding acquisition, Methodology, Supervision, Validation, Writing – review & editing. **Feng Ren:** Conceptualization, Methodology, Writing – review & editing. **Carolina Romero:** Conceptualization, Writing – review & editing. **Javier R. Vázquez de Aldana:** Conceptualization, Funding acquisition, Writing – review & editing. **Yuechen Jia:** Conceptualization, Formal analysis, Funding acquisition, Investigation, Methodology, Project administration, Supervision, Validation, Writing – review & editing. **Feng Chen:** Conceptualization, Funding acquisition, Methodology, Project administration, Resources, Supervision, Validation, Writing – review & editing.

Declaration of Competing Interest

The authors declare that they have no known competing financial interests or personal relationships that could have appeared to influence the work reported in this paper.

References

[1] Bogaerts W, Pérez D, Capmany J, Miller DAB, Poon J, Englund D, et al. Programmable photonic circuits. Nature 2020;586(7828):207–16. https://doi.org/10.1038/s41586-020-2764-0.
[2] Li Mo, Pernice WHP, Xiong C, Baehr-Jones T, Hochberg M, Tang HX. Harnessing optical forces in integrated photonic circuits. Nature 2008;456(7221):480–4. https://doi.org/10.1038/nature07545.
[3] Liu Y, Yan X, Wu J, Zhu B, Chen Y, Chen X. On-chip erbium-doped lithium niobate microcavity laser. Sci China: Phys Mech Astron 2021;64(3):234262. https://doi.org/10.1007/s11433-020-1625-9.
[4] M. Nuck, M. Kleinert, H. Conradi, D. De Felipe, C. Zawadazki, A. Scheu, M. Kresse, W. Brinker, N. Keil and M. Schell, 3D photonic integrated 4x4 multi-mode interference coupler[R]. Conference on Integrated Optics - Devices, Materials, and Technologies XXIII, San Francisco, CA 2019. https://doi.org/10.1117/12.2509776.
[5] Sugioka, Koji. Progress in ultrafast laser processing and future prospects. Nanophotonics 2017;6(2):393–413. https://doi.org/10.1515/nanoph-2016-0004.
[6] Ren Y, Dong N, Chen F, Jaque D. Swift nitrogen ion irradiated waveguide lasers in Nd:YAG crystal. Opt Express 2008;19(6):5522–7. https://doi.org/10.1364/OE.19.005522.
[7] Gross S, Withford MJ. Ultrafast-laser-inscribed 3d integrated photonics: challenges and emerging applications. Nanophotonics 2015;4(3):332–52. https://doi.org/10.1515/nanoph-2015-0020.
[8] Sima F, Sugioka K, Vázquez RM, Osellame R, Kelemen L, Ormos P. Three-dimensional femtosecond laser processing for lab-on-a-chip applications. Nanophotonics 2018;7(3):613–34. https://doi.org/10.1515/nanoph-2017-0097.
[9] Malinauskas M, Žukauskas A, Hasegawa S, Hayasaki Y, Mizeikis V, Buividas R, Juodkazis S. Ultrafast laser processing of materials: from science to industry. Light Sci Appl 2016;5. https://doi.org/10.1038/lsa.2016.133.
[10] Sun X, Sun S, Romero C, Vázquez de Aldana JR, Liu F, Jia Y, et al. Femtosecond laser direct writing of depressed cladding waveguides in Nd:YAG with "ear-like" structures: fabrication and laser generation. Opt Express 2021;29(3):4296. https://doi.org/10.1364/OE.417815.
[11] Jia Y, Chen F. Compact solid-state waveguide lasers operating in the pulsed regime: a review [Invited]. Chin Opt Lett 2019;17(1):012302. https://doi.org/10.3788/col201917.012302.
[12] Benayas A, Silva WF, Ródenas A, Jacinto C, Vázquez de Aldana J, Chen F, et al. Ultrafast laser writing of optical waveguides in ceramic Yb:YAG: a study of thermal and non-thermal regimes. Appl Phys A 2011;104(1):301–9. https://doi.org/10.1007/s00339-010-6135-9.
[13] Chen F, De Aldana JRV. Optical waveguides in crystalline dielectric materials produced by femtosecond-laser micromachining. Laser Photonics Rev 2014;8(2):251–75. https://doi.org/10.1002/lpor.201300025.
[14] Okhrimchuk AG, Mezentsev V, Shestakov A, Bennion L. Low loss depressed cladding waveguide inscribed in YAG: Nd single crystal by femtosecond laser pulses. Opt Express 2012;20(4):3832–43. https://doi.org/10.1364/OE.20.003832.
[15] Okhrimchuk AG, Shestakov AV, Khrushchev I, Mitchell J. Depressed cladding, buried waveguide laser formed in a YAG:Nd^{3+} crystal by femtosecond laser writing. Opt Lett 2005;30(17):2248–50. https://doi.org/10.1364/OL.30.002248.
[16] Jia Y, He R, de Aldana JRV, Liu H, Chen F. Femtosecond laser direct writing of few-mode depressed-cladding waveguide lasers. Opt Express 2019;27(21):30941–51. https://doi.org/10.1364/OE.27.030941.
[17] Jia Y, Wang S, Chen F. Femtosecond Laser Direct Writing of Flexibly Configured waveguide geometries in optical crystals: fabrication and application. Opto-Electron Adv 2020;3(10):190042. https://doi.org/10.29026/oea.2020.190042.
[18] Li L, Li Z, Nie W, Romero C, de Aldana JRV, Chen F. Femtosecond-laser-written S-curved waveguide in Nd:YAP crystal: fabrication and multi-gigahertz lasing. J Lightwave Technol 2020;38(24):6845–52. https://doi.org/10.1109/JLT.5010.1109/JLT.2020.3015690.
[19] Ajates JG, de Aldana JRV, Chen F, Rodenas A. Three-dimensional beam-splitting transitions and numerical modelling of direct-laser-written near-infrared $LiNbO_3$ cladding waveguides. Opt Mater Express 2018;8(7):1890–901. https://doi.org/10.1364/OME.8.001890.
[20] Li L, Nie W, Li Z, Romero C, Rodriguez-Beltrán RI, Vázquez de Aldana JR, et al. Laser-writing of ring-shaped waveguides in BGO crystal for telecommunication band. Opt Express 2017;25(20):24236. https://doi.org/10.1364/OE.25.024236.
[21] Romero C, Ajates J, Chen F, de Aldana JRV. Fabrication of tapered circular depressed-cladding waveguides in Nd:YAG crystal by femtosecond-laser direct inscription. Micromachines 2020;11(1):10. https://doi.org/10.3390/mi11010010.
[22] Ishaaya A, Oron R, Davidson N, Hasman E, Friesem A. "Improving the beam quality of high-order laser modes. Opt Photonics News 2001;12(12):55. https://doi.org/10.1364/OPN.12.12.000055.
[23] Balaji VR, Murugan M, Robinson S, Hegde G. Design and analysis of waveguide taper for photonic crystal demultiplexer. Silicon 2020. https://doi.org/10.1007/s12633-020-00678-w.
[24] Lee S, Son D, Kwon JY, Park YB. Analysis of a tapered rectangular waveguide for V to W millimeter wavebands. J Electromagn Eng Sci 2018;18(4):248–53. https://doi.org/10.26866/jees.2018.18.4.248.
[25] Brandus C-A, Greculeasa M, Broasca A, Voicu F, Gheorghe L, Pavel N. Diode-pumped bifunctional Nd:LGSB laser passively Q-switched by a Cr^{4+}:YAG saturable absorber. Opt Mater Express 2021;11(3):685. https://doi.org/10.1364/OME.416425.
[26] Keller U. Recent developments in compact ultrafast lasers. Nature 2003;424(6950):831–8. https://doi.org/10.1038/nature01938.
[27] Li Z, Zhang Y, Cheng C, Yu H, Chen F. 6.5 GHz Q-Switched Mode-Locked Waveguide lasers based on two-dimensional materials as saturable absorbers. Opt Express 2018;26(9):11321–30. https://doi.org/10.1364/OE.26.011321.
[28] Li Z, Dong N, Cheng C, Xu L, Chen M, Wang J, et al. Enhanced nonlinear optical response of graphene by silver-based nanoparticle modification for pulsed lasing. Opt Mater Express 2018;8(5):1368. https://doi.org/10.1364/OME.8.001368.
[29] Li Z, Li R, Chi P, Zhang Y, Yu H, Feng C. WSe2 as a saturable absorber for multi-gigahertz Q-switched mode-locked waveguide lasers [invited]. Chin Opt Lett 2019;17(2). https://doi.org/10.3788/COL201917.020013.
[30] Tan Y, Zhang H, Zhao C, Akhmadaliev S, Chen F. Bi_2Se_3 Q-switched Nd:YAG ceramic waveguide laser. Opt Lett 2015;40(4):637–40. https://doi.org/10.1364/OL.40.000637.
[31] Zhang B, Sato R, Momida H, Ohno T, Chundak M, Naito M, et al. Spectral dependence of the third-order optical susceptibility of Au nanostructures: experiments and first-principles calculations. Phys Rev B 2019;100(3). https://doi.org/10.1103/PhysRevB.100.035446.
[32] Yraola E, Molina P, Plaza JL, Ramírez MO, Bausá LE. Spontaneous emission and nonlinear response enhancement by silver nanoparticles in a Nd^{3+}-doped periodically poled $LiNbO_3$ laser crystal. Adv Mater 2013;25(6):910–5. https://doi.org/10.1002/adma.v25.610.1002/adma.201203176.
[33] Li R, Pang C, Li Z, Yang M, Amekura H, Dong N, et al. Fused silica with embedded 2D-like Ag nanoparticle monolayer: tunable saturable absorbers by interparticle spacing manipulation. Laser Photonics Rev 2020;14(2):1900302. https://doi.org/10.1002/lpor.v14.210.1002/lpor.201900302.
[34] Wang X-D, Luo Z-C, Liu H, Liu M, Luo A-P, Xu W-C. Microfiber-based gold nanorods as saturable absorber for femtosecond pulse generation in a fiber laser. Appl Phys Lett 2014;105(16):161107. https://doi.org/10.1063/1.4899133.
[35] Pang C, Li R, Li Z, Dong N, Cheng C, Nie W, et al. Mode-locked lasers: lithium niobate crystal with embedded Au nanoparticles: a new saturable absorber for efficient mode-locking of ultrafast laser pulses at 1 μm (Advanced Optical Materials 16/2018). Adv Opt Mater 2018;6(16):1870065. https://doi.org/10.1002/adom.v6.1610.1002/adom.201870065.
[36] Politi A, Cryan MJ, Rarity JG, Yu S, O'Brien JL. Silica-on-silicon waveguide quantum circuits. Science 2008;320(5876):646–9. https://doi.org/10.1126/science.1155441.

[37] Frederik K, Norbert S, Andreas S, Andre W, Nico K, Matthias W, et al. Nanocomposites: glassomer-processing fused silica glass like a polymer. Adv Mater 2018;30(22):1870151. https://doi.org/10.1002/adma.201870151.
[38] Matthews JCF, Politi A, Stefanov A, O'Brien JL. Manipulating multi-photon entanglement in waveguide quantum circuits. Nat Photonics 2009;3:346–50. https://doi.org/10.1038/nphoton.2009.93.
[39] Kotz F, Arnold K, Bauer W, Schild D, Keller N, Sachsenheimer K, et al. Three-dimensional printing of transparent fused silica glass. Nature 2017;544(7650): 337–9. https://doi.org/10.1038/nature22061.